

SurfAge-Net: A Hierarchical Surface-Based Network for Interpretable Fine-Grained Brain Age Prediction

Rongzhao He, Dalin Zhu, Ying Wang, Songhong Yue, Leilei Zhao, Yu Fu, Dan Wu, Bin Hu, *Fellow, IEEE*, Weihao Zheng, *Member, IEEE*

Abstract—Brain age prediction serves as a powerful framework for assessing brain status and detecting deviations associated with neurodevelopmental and neurodegenerative disorders. However, most existing approaches emphasize whole-brain age prediction and therefore overlook the pronounced regional heterogeneity of brain maturation that is crucial for detecting localized atypical trajectories. To address this limitation, we propose a novel spherical surface-based brain age prediction network (SurfAge-Net) that leverages multiple morphological metrics to capture region-specific developmental patterns with enhanced robustness and clinical interpretability. SurfAge-Net establishes a new modeling paradigm by incorporating the connectomic principles of cortical organization: it explicitly models both intra- and inter-hemispheric dependencies through a spatial-channel mixing and a lateralization-aware attention mechanism, enabling the network to characterize the coordinate maturation pattern uniquely associated with each target region. Validated on three fetal and neonatal datasets, SurfAge-Net outperforms existing approaches (global MAE = 0.54, regional MAE = 0.45 in gestational/postmenstrual weeks) and demonstrates strong generalizability across external cohorts. Importantly, it provides spatially precise and biologically interpretable maps of cortical maturation, effectively identifying heterogeneous delays and regional-specific abnormalities in atypical developmental populations. These results established fine-grained brain age prediction as a promising paradigm for advancing neurodevelopmental research and supporting early clinical assessment.

This work was supported in part by the National Natural Science Foundation of China under Grant 62227807 and 62202212, in part by the Gansu Provincial Health Commission Scientific Research Program of China under Grant GWSKY2023-35. (Rongzhao He and Dalin Zhu contribute equally to this work.) (Corresponding author: Weihao Zheng; Dan Wu; Bin Hu.)

This work involved human subjects or animals in its research. Approval of all ethical and experimental procedures and protocols was granted by the Ethics Committee of Gansu Provincial Maternity and Child-Care Hospital under Application No. 2020-GSFY-05 and Lanzhou University Second Hospital under Application No. 2021A-601.

Rongzhao He, Ying Wang, Yu Fu, and Weihao Zheng are with the Gansu Provincial Key Laboratory of Wearable Computing, School of Information Science and Engineering, Lanzhou University, Lanzhou 730000, China (e-mail: herongzhao23@lzu.edu.cn; wangying22@lzu.edu.cn; fuyu@lzu.edu.cn; zhengweihao@lzu.edu.cn).

Dalin Zhu is with the Department of Medical Imaging Center, Gansu Provincial Maternity and Child-Care Hospital, Lanzhou 730050, China (e-mail: zdlddz@126.com).

Songhong Yue is with the Department of Magnetic Resonance, Lanzhou University Second Hospital, Lanzhou 730030, China (e-mail: ysh-wjt@163.com).

Leilei Zhao is with the Department of Computer Science and Technology, Harbin Institute of Technology (Shenzhen), Shenzhen 518055, China (e-mail: 24B951025@stu.hit.edu.cn).

Dan Wu is with the Key Laboratory for Biomedical Engineering of Ministry of Education, Department of Biomedical Engineering, College of Biomedical Engineering & Instrument Science, Zhejiang University, Hangzhou 310027, China (e-mail: danwu.bme@zju.edu.cn).

Bin Hu is with the Gansu Provincial Key Laboratory of Wearable Computing, School of Information Science and Engineering, Lanzhou University, Lanzhou 730000, China, also with the School of Medical Technology, Beijing Institute of Technology, Beijing 100081, China (e-mail: bh@lzu.edu.cn).

Index Terms—Cortical spherical surface, Fine-grained, Brain age prediction, Fetal and neonatal, Morphological metrics, Interpretability.

I. INTRODUCTION

THE human brain undergoes a complex and dynamic, and highly organized developmental process [1], [2]. Among the biological indicator used to characterize this trajectory, brain age has emerged as a valuable marker reflecting the structural and functional maturity of the brain [3], [4]. By comparing predicted brain age with chronological age, researchers can quantify deviations from normative developmental patterns, which are often associated with neurodevelopmental and neurodegenerative conditions [5], [6]. For example, accelerated brain development and aging have been linked to autism spectrum disorder [6] and Alzheimer's disease [7], respectively; whereas delayed brain maturation is commonly observed in preterm infants [8], [9], which provides only a global summary of brain maturity and fails to account for substantial regional diversity of developmental trajectories [10], [11], [12], [13]. As a result, subtle but clinically meaningful regional deviations may be masked when aggregated across the entire brain.

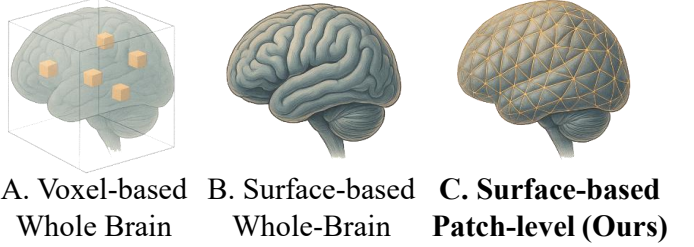
Accumulating evidence indicates that brain maturation progresses in a markedly regionally heterogeneous manner. Under typical development, cortical maturation follows a unimodal-to-transmodal gradient, with primary cortices (e.g., primary sensory and motor regions) and their associated white-matter tracts mature earlier during late gestation and early infancy, while higher-order association regions (e.g., default mode and salience networks) mature substantially later [1], [13], [14]. However, this maturational gradient is often disrupted in atypical developmental populations. For example, preterm infants show selectively delayed neurite maturation in posterior cortical regions but accelerated development of cortical thickness in anterior cortex compared to term newborns [9]. Similarly, abnormal expansion of prefrontal surface area has been observed in high-risk infants who were diagnosed with autism at 24 months [6]. Such regional variability during atypical development may lead to region-specific deviations in developmental status that cannot be adequately captured by a global brain-age model, thereby underscoring the need for spatially resolved models capable of quantifying localized cerebral maturity.

Nevertheless, despite this widely demonstrated regional developmental heterogeneity, most existing approaches remain confined to estimating a single global brain-age value [15]. While such a global metric provides a concise summary of

overall brain maturation, it inevitably collapses the diverse regional developmental trajectories distributed across the cortex. This spatial averaging may obscure clinical meaningful deviation, e.g., accelerated maturation in anterior cortex of preterm infants, that are closely associated with subsequent cognitive development, functional specialization, and domain-specific behavioral outcomes. In addition, previous studies have predominantly emphasized model interpretability, typically achieved through visualizing feature contribution or attention weights for the prediction [16], [17]. However, this form of interpretability does not necessarily translate into clinical interpretability, which concerns *where, in what direction, and to what extent* an individual's brain development deviates from normative trajectories, as well as the potential cognitive or behavioral implications of such deviations. Therefore, the clinical utility and risk-assessment relevance of global brain age remain inherently limited, motivating a growing interest in fine-grained brain-age estimation. For example, several studies have attempted voxel-level brain-age prediction [18], [19]. While these approaches markedly enhance spatial resolution relative to whole-brain estimates, the extremely high dimensionality of voxel-wise representations significantly increases the risk of overfitting and computational burden. Moreover, voxel-level predictions are highly sensitive to noise or preprocessing variability (e.g., registration inaccuracies and spatial smoothing effects), which further weakened their robustness. These limitations indicate that finer granularity is not inherently advantageous. Instead, it is essential to define an appropriate representational scale that balances predictive precision, spatial resolution, computational efficiency, and model robustness.

Surface-based morphometry (SBM) has become a powerful tool for characterizing cortical morphology. By mapping the highly convoluted cortex onto a spherical surface, SBM enables more accurate quantification of complex geometric structures and folding patterns. Compared to voxel-based morphometry (VBM), SBM offers improved cortical alignment and parcellation, which reduces errors introduced by complex gyral-sulcal topography, and provides a richer set of morphological descriptors, such as cortical thickness, sulcal depth, and curvature, that jointly capture complementary aspects of cortical shape [20]. Recent studies have demonstrated strong age-related changes in these features, each exhibiting distinct developmental or aging trajectories across the lifespan [21], [22]. Such feature-specific heterogeneity is especially pronounced during the first year of life, a period marked by rapid and highly nonuniform cortical growth [23], [24]. Given that SBM depicts multiple dimensions of cortical morphology that are often missing in voxel-based representation, it may provide a more comprehensive and biologically sensitive basis for brain age estimation. In fact, recent studies have shown the effectiveness of employing multiple SBM metrics for this purpose, particularly in the neonatal cohort [16], [25], [26], supporting the potential of SBM to enable more precise characterization of brain maturational status, especially when the goal is to capture subtle, spatially localized developmental patterns.

In the present study, we propose a patch-level brain age



A. Voxel-based Whole Brain **B. Surface-based Whole-Brain** **C. Surface-based Patch-level (Ours)**

Fig. 1. Different brain age prediction paradigms.

prediction paradigm based on cortical surface data, termed SurfAge-Net. An overview of different brain age prediction paradigms is illustrated in Fig. 1. The primary aim of SurfAge-Net is to enhance the clinical interpretability of brain-age estimates by providing a spatially resolved mapping of maturational heterogeneity throughout the cortex, meanwhile maintaining satisfied prediction accuracy. To achieve this goal, we introduce a connectome-inspired modeling strategy that allows the age of each cortical patch to be predicted not only from its own morphological metrics but also from its intrinsic interactions with anatomically related regions. Specifically, we design a Spatial-Channel Mixing Block to facilitate effective information exchange among intra-hemispheric neighboring patches, and incorporate a Lateralization-Aware Attention Mechanism to selectively integrate contralateral information. In addition, a Gated Filter Module is introduced, which adaptively balance ipsilateral and contralateral contributions while suppressing irrelevant patches, reflecting the brain connectivity principles that cortical areas typically interact with a subset of structurally or functionally meaningful partners [27], [28]. These components enable SurfAge-Net to learn biologically informed inter-regional dependencies that are essential for precise and clinically meaningful patch-level brain-age estimation. The main contributions of this work are summarized as follows:

- 1) We introduce SurfAge-Net, the first spherical-surface-based patch-level prediction framework for fine-grained brain-age estimation, enabling high-resolution assessment of cerebral regional maturity.
- 2) SurfAge-Net achieves state-of-the-art performance in both global and regional brain-age prediction and demonstrates strong generalizability across multiple external cohorts.
- 3) SurfAge-Net substantially enhances clinical interpretability by generating spatially resolved cortical age maps that uncover localized maturational deviations in atypically developing populations.

II. RELATED WORK

A. Global Brain Age Prediction

Early research on global brain-age prediction primarily relied on statistical learning models with handcrafted features [29], [30], [31], [32], [33]. These works demonstrated the feasibility of using brain age as a biomarker for neurodevelopmental and neurodegenerative conditions, yet their predictive

TABLE I
DEMOGRAPHIC INFORMATION OF PARTICIPANTS USED IN OUR STUDY.

	<i>dHCP</i> (N=1166)	<i>GSMCH</i> (N=65)	<i>LZUSH</i> (N=49)
Birth age [weeks ^{+days}], median (IQR)	37 ⁺² (34 ⁺⁶ -40 ⁺⁴)	33 ⁺³ (30 ⁺⁴ -36 ⁺⁴)	-
Scan age [weeks ^{+days}], median (IQR)	37 ⁺⁴ (34 ⁺⁰ -42 ⁺⁰)	38 ⁺³ (36 ⁺¹ -40 ⁺²)	29 ⁺⁶ (28 ⁺⁰ -32 ⁺⁰)
Birth weight ¹ , mean (SD)	2.83 (0.96)	1.95 (0.86)	-
Head circumference at scan ² , mean (SD)	34.16 (2.81)	32.90 (3.28)	-
Radiology score (1/2/3/4/5)	716/257/122/55/16	-	-
Gender ³ (M/F)	631/533	34/31	-/-

¹ 1 and 2 birth weight data was missed in *dHCP* and *GSMCH*, respectively.

² 34 and 37 head circumference data were missed in *dHCP* and *GSMCH*, respectively.

³ Gender information was unavailable for 2 fetuses in *dHCP*.

performance remained limited due to shallow learning ability and the restricted expressiveness of manually engineered features. With the rise of deep learning, convolutional neural networks (CNNs) and their variants [18], [34], [35], [36], [37], [38] enabled end-to-end modeling of volumetric MRI, substantially improving performance. More recently, geometric deep learning (GDL) has extended brain-age predictions to non-Euclidean domains, including cortical surfaces and brain connectivity graphs [17], [39], [40], [41], [42], [43], [44], [45], [46], enabling more faithful representation of the intrinsic topology of brain. Attention-based architectures have further strengthened the modeling of long-range dependencies [16], [26], [47], [48], and the emerging state space models (e.g. Mamba) [49] have provided a favorable trade-off between predictive performance and computational efficiency. Despite this methodological progress, global prediction frameworks collapse the complex spatial heterogeneity of neurodevelopmental into a single scalar measure. Therefore, they are inherently limited in capturing localized maturational deviations that are critical for understanding heterogeneous developmental process and disease-specific brain alterations.

B. Fine-Grained Brain Age Prediction

Early efforts towards fine-grained brain-age estimation largely relied on linear regression [50], most notably voxel-wise prediction through fitting independent linear models [51]. However, such approaches ignored contextual dependencies and fail to capture the inter-regional structural coherence that underpin cortical development. Moreover, accumulating evidence shows that brain maturation follows regionally distinct and often non-linear trajectories [52], [53], exceeding the representational capacity of linear models. The introduction of deep learning brought significant progress. A U-Net-based voxel-wise framework [54] generated spatially resolved brain age maps that revealed disease-related patterns, such as elevated age gaps in hippocampal and basal ganglia regions in individuals with mild cognitive impairment or dementia. More recently, Gianchandani *et al.* [55] extended this line of work with a multi-task U-Net that jointly predicted both voxel-level and global brain age while performing tissue segmentation, thereby enhancing interpretability. Despite these advances, voxel-level approaches face several fundamental limitations. First, voxel-based morphometry primarily captures volumetric information and struggles to represent cortical geometry, such as folding patterns, which are more naturally captured on

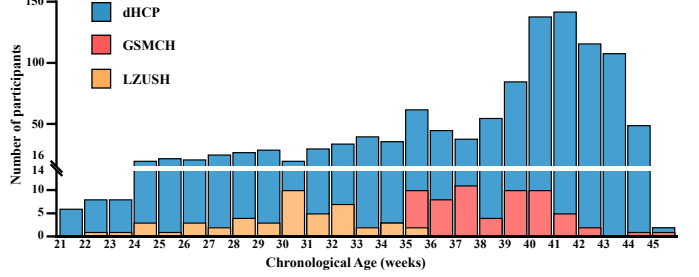


Fig. 2. The distribution of chronological ages for all participants utilized in this study.

the cortical surface. Second, voxel-wise representations are extremely high dimensional, requiring large training datasets and substantial computational resources, and may also increase the risk of overfitting and reduce the robustness to noise and motion artifacts. These challenges highlight the need for a method that adopt an appropriate scale and meaningful feature representation to enable more reliable fine-grained brain-age prediction.

III. MATERIALS AND METHODS

A. Imaging Data

Three datasets, with a total of 1280 fetal and neonatal MRIs, were used in this study: (i) the fourth data release of the publicly available Developing Human Connectome Project (*dHCP*), which includes 1166 MRI scans of both neonates and fetuses; (ii) 65 neonatal brain MRI data collected from the Gansu Provincial Maternity and Child-Care Hospital (*GSMCH*); and (iii) 49 fetal brain MRI data collected from the Lanzhou University Second Hospital (*LZUSH*). The demographic information of the three cohorts is summarized in Table I, and the distribution of chronological ages for all participants utilized in this study is visualized in Fig. 2.

Images for the *dHCP* dataset were acquired on a 3.0 T Philips Achieva scanner equipped with a 32-channel neonatal head coil. For the *GSMCH* dataset (approved by ethics committee of *GSMCH*, No. 2020-GSFY-05) were acquired using a Siemens Magnetom Lumina 3.0 T scanner with a spin echo (SE) sequence. The imaging resolution for both datasets was $0.8 \times 0.8 \times 1.6 \text{ mm}^3$ with 0.8 mm overlap, and all images were reconstructed to an isotropic resolution of 0.5 mm. For the *LZUSH* dataset (approved by ethics committee of *LZUSH*, No. 2021A-601), T2-weighted (T2w) fetal brain

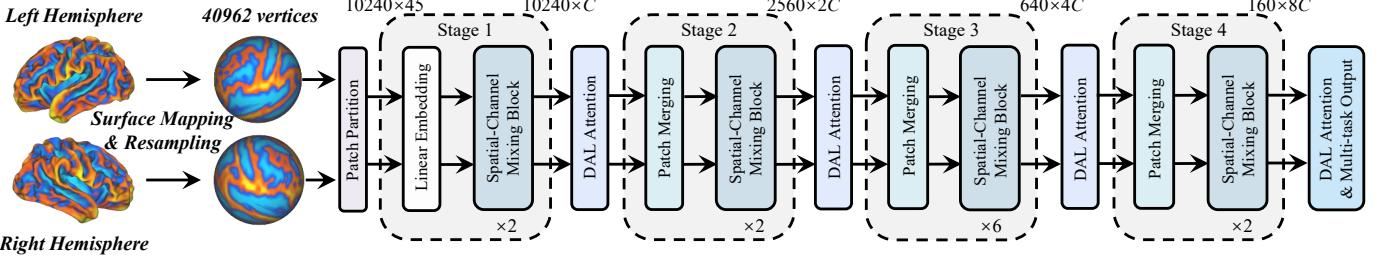


Fig. 3. Overview of the SurfAge-Net architecture.

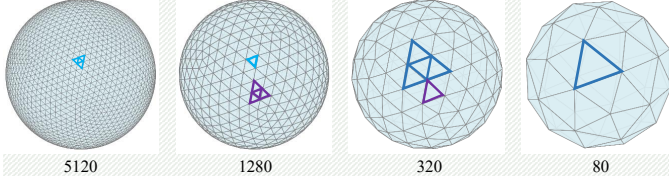


Fig. 4. Patch merging process. The number of faces of each spherical surface is denoted under the surface.

MRI data were acquired using Single-shot Fast Spin Echo (SSFSE) sequence on a Philips Ingenia 3.0 T scanner. To mitigate motion artifacts, each fetal brain was scanned multiple times in three orthogonal planes (axial, coronal and sagittal), with a repetition time of 12,000 ms, an echo time of 80 ms, a matrix size of 236×220 , a flip angle of 90° , a field of view of 260×355 mm 2 , slice thickness of 2 mm with no gap, and a scan time ranging from 15 to 45 s. As the data were obtained as thick-slice 2D stacks, super-resolution reconstruction was required to generate a high-resolution 3D volume, and the detailed procedure is described in Section III-B.

To construct a normative model of typical brain development during the second and third trimesters, we selected fetal and neonatal images from the *dHCP* dataset based on the following criteria: (i) only the first scan of each fetus/neonate was retained; (ii) term-born neonates scanned within one week after birth, with no focal abnormalities (radiology score < 4). A total of 976 images were obtained and divided into training, validation, and test sets with a ratio of 8:1:1 within each label interval for training in each infant and fetal group. Subsequently, the best-performed model was applied to several atypical developmental groups to investigate brain developmental characteristics under different atypical conditions, including: (i) 66 and 24 moderate-to-late preterm (32-37 weeks) from *dHCP* and *GSMCH*, respectively; (ii) 53 and 25 extremely preterm (24-32 weeks) from *dHCP* and *GSMCH*, respectively; (iii) 71 focal abnormalities (radiology score > 3) from *dHCP*.

B. Data Preprocessing

Motion-corrected T2w images underwent cortical reconstruction using the *dHCP* neonatal structural pipeline [56]. This framework integrates probabilistic tissue segmentation via Draw-EM [57] with surface topology derivation and refinement [58], followed by generation of anatomically consistent inner (white matter), outer (pial), midthickness, inflated and

spherical surface representations with vertex-wise correspondence across subjects. In addition, the pipeline yields multiple cortical surface phenotypes characterising morphology and folding architecture, including cortical thickness, sulcal depth and mean curvature. A full methodological description of image reconstruction and neonatal-specific preprocessing is detailed in Makropoulos *et al.* [56].

For the *LZUSH* dataset, super-resolution reconstruction was performed to generate high-resolution 3D fetal brain volumes. The procedure was as follows. First, fetal brain masks were obtained using the NiftyMIC pipeline (<https://github.com/gift-surg/NiftyMIC>) based on multi-planar 2D stacks (axial, coronal and sagittal). Next, the masked stacks were used for super-resolution reconstruction, producing a 3D fetal brain volume with 0.8 mm isotropic resolution. The intracranial region was then extracted using the reconstructed brain mask, followed by manual AC-PC alignment of the 3D MRI volume in MATLAB using SPM.

All data were registered to the *dHCP* 36-week spherical template, which represents the cortical surface as an approximated sphere composed of triangles, with 32,492 vertices per hemisphere. We resampled the template sphere to a regular sixth-order icosphere (Ico-6) using barycentric interpolation. Morphological metrics, including mean curvature, sulcal depth, and thickness of cerebral cortex, were calculated from T2w images. Each feature channel was normalized using Z-score.

C. Network Architecture

As shown in Fig. 3, SurfAge-Net incorporates a novel and well-suited Spatial-Channel mixing block (SCM) and Dynamic Adaptive Lateralization-Aware Attention (DALA), dedicated to intra-hemispheric and inter-hemispheric modeling, respectively. The SCM block enables information exchange among cortical regions within each hemisphere while simultaneously enhancing the feature representation of each region. In contrast, the DALA module models cross-hemispheric interactions between the left and right hemispheres, effectively characterizing the lateralized developmental structure of brain and improving prediction performance.

To be more specific, the cortical surface was partitioned into $2N$ patches, denoted as $\tilde{X} = \{\tilde{L}, \tilde{R} | \tilde{L} \in \mathbb{R}^{N \times V \times C}, \tilde{R} \in \mathbb{R}^{N \times V \times C}\}$, where V is the number of vertices per patch and C is the number of feature channels. Each patch was then flattened into $X = \{L, R | L \in \mathbb{R}^{N \times (VC)}, R \in \mathbb{R}^{N \times (VC)}\}$, with $L = [X_L^1, X_L^2, \dots, X_L^N]$ and $R = [X_R^1, X_R^2, \dots, X_R^N]$.

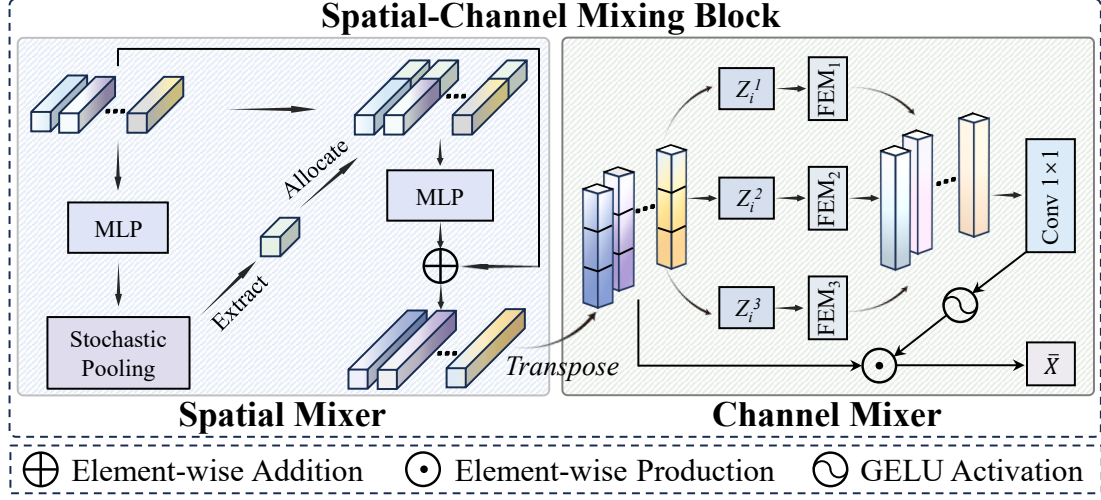


Fig. 5. The detailed structures of the Spatial-Channel Mixing Block.

These representations were processed by a four-stage hierarchical network. The first stage applied a linear embedding to project inputs into feature space, while the remaining three stages began with a patch-merging layer for progressive spatial reduction (shown in Fig. 4). The input data were first partitioned into 10,240 non-overlapping triangular patches using an Ico-4 spherical grid. After patch-merging operations in the last three stages, the network aggregated these into 160 cortical regions comprising 80 regions per hemisphere. Each stage consisted of a SCM block and a DALA block. The SCM block integrates information across patches within the same hemisphere to capture intra-hemispheric dependencies, and the DALA block models inter-hemispheric interactions to capture long-range structural associations in a lateralization-aware manner. Finally, SurfAge-Net employed a multi-task prediction head. Each of the 160 cortical regions was assigned an independent linear layer to estimate its regional brain age, while an additional linear layer was dedicated to whole-brain age prediction. This design encourages shared representations that jointly benefit regional and global predictions, improving robustness against local noise and interpretability in developmental assessment.

D. Spatial-Channel Mixing Block

The human brain exhibits strong structural lateralization, with hemisphere-specific morphometric patterns in cortical thickness, sulcal depth, and curvature. These patterns are not uniformly distributed but instead follow hemisphere-specific folding architectures and developmental constraints. To preserve these signatures, we first performed intra-hemispheric modeling by aggregating hemisphere-level information and enhancing patch-wise features for regional brain age prediction. An MLP-based design was employed for spatial-channel mixing, achieving linear complexity with respect to the number of patches and avoiding the computational burden of global attention. The detailed structure of SCM is shown in Fig. 5.

1) *Spatial Mixer*: The Spatial Mixer is designed as a resource-efficient module for global information aggregation within each hemisphere. Given the patch-wise feature representation X , we first projected the input into D -dimensional vectors using a parameterized MLP. To obtain a hemisphere-level summary, we applied stochastic pooling across the N patches. For each feature dimension j , the selection probability of patch i is defined by softmax normalization:

$$p_{ij} = \frac{e^{x_{ij}}}{\sum_{k=1}^N e^{x_{ik}}} \quad (1)$$

where, x is L or R ; stochasticity is introduced by sampling one patch index c from the Categorical distribution parameterized by the probabilities during training:

$$o_j = x_{cj}, \quad c \sim \text{Categorical}(p_{1j}, p_{2j}, \dots, p_{Nj}) \quad (2)$$

where ‘‘Categorical’’ denotes a discrete probability distribution parameterized by the vector $(p_{1j}, p_{2j}, \dots, p_{Nj})$. The stochastic sampling introduces randomness during training, acting as a form of regularization that encourages robust representations learning. At inference time, however, stochastic sampling would lead to non-deterministic outputs, therefore we replaced it with its mathematical expectation to ensure consistency and reproducibility:

$$o_j = \sum_{i=1}^N p_{ij} x_{ij} \quad (3)$$

The pooled outputs across all feature dimensions were concatenated to form the Global Representation (GR):

$$GR = [o_1, o_2, \dots, o_{D'}] \in \mathbb{R}^{1 \times D'} \quad (4)$$

To enhance information interactions within each hemisphere, the GR was concatenated with each patch features:

$$\tilde{x}_i = MLP([x_i || GR]) \quad (5)$$

where $||$ denotes concatenation. Finally, residual connections were applied to avoid gradient diminishing:

$$x'_i = x_i + \tilde{x}_i \quad (6)$$

2) *Channel Mixer*: Following spatial aggregation, we employed a Channel Mixer to enhance representational power at the patch level. Inspired by the multi-head attention mechanism, we split each patch feature vector into three disjoint channel groups, enabling complementary specialization across channels and improving the encoding of fine-grained details. Formally, we transposed the outputs to reorganize features along the feature dimension, yielding the representation:

$$Z = [z_1, z_2, \dots, z_N], \quad z_i \in \mathbb{R}^{1 \times D} \quad (7)$$

where z_i denotes the feature of the i -th patch. To further enrich patch-level representations, we uniformly divided the feature channels of each patch into three disjoint subspaces, which were processed through a Feature Enhancement Module (FEM):

$$z_i = [z_i^{c_1}, z_i^{c_2}, z_i^{c_3}], \quad z_i^{c_m} \in \mathbb{R}^{1 \times \frac{D}{3}}, \quad m = 1, 2, 3 \quad (8)$$

For each subspace, we apply an independent transformation function $f_m(\cdot)$. The first group was processed directly using a depthwise convolution:

$$f_1(z_i^{c_1}) = DWConv_1(z_i^{c_1}) \quad (9)$$

The remaining two groups were processed in a multi-scale manner. Each subset was adaptively pooled to a reduced dimension p_m , and then upsampled back to the original feature length via nearest-neighbor interpolation:

$$f_m(z_i^{c_m}) = Up_{\uparrow \frac{D}{3}}(DWConv(Pool_{\downarrow p_m}(z_i^{c_m}))), \quad m = 2, 3 \quad (10)$$

where $Pool_{\downarrow p_m}(\cdot)$ represents adaptive max pooling and $Up_{\uparrow \frac{D}{3}}(\cdot)$ restores the channel dimension to $\frac{D}{3}$.

The transformed groups were concatenated and aggregated to form the enhanced patch representation:

$$h_i = Conv([f_1(z_i^{c_1}) \| f_2(z_i^{c_2}) \| f_3(z_i^{c_3})]) \quad (11)$$

Finally, a nonlinear activation was applied to the aggregated features, which were then modulated with the original input through element-wise multiplication:

$$\tilde{h}_i = GELU(h_i) \odot z_i \quad (12)$$

where \odot denotes element-wise multiplication. Collecting all patch features within the left and right hemispheres yields:

$$\begin{aligned} Z^L &= [\tilde{h}_1^L, \tilde{h}_2^L, \dots, \tilde{h}_N^L] \in \mathbb{R}^{N \times D}, \\ Z^R &= [\tilde{h}_1^R, \tilde{h}_2^R, \dots, \tilde{h}_N^R] \in \mathbb{R}^{N \times D} \end{aligned} \quad (13)$$

E. Dynamic Adaptive Lateralization-Aware Attention

While structural lateralization differentiates the two hemispheres, the brain also maintains inter-hemispheric relationships through homotopic correspondences and complementary asymmetries. We introduced inter-hemispheric modeling to explicitly capture cross-hemispheric dependencies. To this end, we employed a cross-attention mechanism that selectively integrates information between hemispheres (Fig. 6). By restricting attention to contralateral interactions, rather than all patches across the brain, we achieved computational efficiency

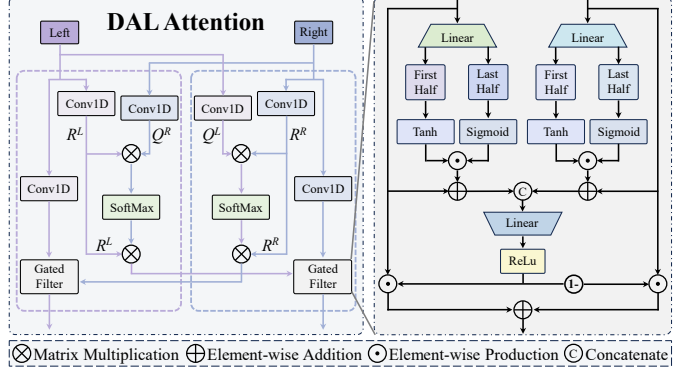


Fig. 6. The detailed structures of the Dynamic Adaptive Lateralization-Aware Attention.

while enabling the network to learn crucial asymmetry- and integration-related patterns.

Specifically, features of each hemisphere were projected into Embedding, Query, and Reference tokens:

$$\begin{aligned} E^L &= Conv_{1 \times 1}(Z^L), & E^R &= Conv_{1 \times 1}(Z^R), \\ Q^L &= Conv_{1 \times 1}(Z^L), & Q^R &= Conv_{1 \times 1}(Z^R), \\ R^L &= Conv_{1 \times 1}(Z^L), & R^R &= Conv_{1 \times 1}(Z^R) \end{aligned} \quad (14)$$

where the Reference token replaces both keys and values, reducing parameter redundancy and computational cost while enforcing a unified representational space for similarity measurement and information aggregation. This design is particularly beneficial for modeling cross-hemispheric relationships, where structural symmetry and homotopic correspondences are essential.

Cross-attention between hemispheres is formulated as:

$$\begin{aligned} \hat{Z}^L &= SoftMax\left(\frac{Q^L(R^R)^T}{\sqrt{D}}\right) R^R, \\ \hat{Z}^R &= SoftMax\left(\frac{Q^R(R^L)^T}{\sqrt{D}}\right) R^L \end{aligned} \quad (15)$$

To further accommodate hemispheric lateralization of the brain, we designed a gated filter module that adaptively balanced hemispheric-specific and contralateral information. Query attends to its contralateral Reference feature were fused with original hemispheric features, allowing dominant intra-hemisphere characteristics to be preserved while adaptively incorporating complementary inter-hemispheric information. The process is formulated as:

$$\begin{aligned} \hat{Z}_1^L &\in \mathbb{R}^{N \times D}, \quad \hat{Z}_2^L \in \mathbb{R}^{N \times D} = \text{Split}(\text{Linear}(\hat{Z}^L)) \\ E_1^L &\in \mathbb{R}^{N \times D}, \quad E_2^L \in \mathbb{R}^{N \times D} = \text{Split}(\text{Linear}(E^L)) \end{aligned} \quad (16)$$

$$\begin{aligned} W^L &= \text{ReLU}\left(\text{Linear}[(\text{Tanh}(\hat{Z}_1^L) \odot \text{Sigmoid}(\hat{Z}_2^L) + \hat{Z}^L) \right. \\ &\quad \left. \| (\text{Tanh}(E_1^L) \odot \text{Sigmoid}(E_2^L) + E^L)]\right) \end{aligned} \quad (17)$$

$$\text{Output}^L = W^L \odot \hat{Z}^L + (1 - W^L) \odot E^L \quad (18)$$

By symmetry, the same process was applied to the other hemisphere to obtain W^R and Output^R .

TABLE II
PERFORMANCE COMPARISON OF DIFFERENT NETWORKS.

Methods	Global MAE	Global PCC	Global SRCC	Region MAE	Region PCC	Region SRCC	Params. (M)
MoNet	0.66±0.47	0.99±0.00	0.96±0.01	-	-	-	-
S2CNN	0.67±0.49	0.99±0.00	0.96±0.01	-	-	-	-
ChebNet	0.67±0.54	0.99±0.00	0.96±0.01	-	-	-	-
GConvNet	0.84±0.82	0.98±0.01	0.91±0.03	-	-	-	-
PointNet++	0.59±0.51	0.99±0.00	0.97±0.01	-	-	-	-
Spherical UNet	0.80±0.84	0.98±0.01	0.92±0.03	-	-	-	-
HRINet/1	0.60±0.45	0.99±0.00	0.97±0.01	-	-	-	9.87
SiT-Small/1	0.63±0.52	0.99±0.00	0.96±0.01	-	-	-	21.99
SiM-Small/1	0.59±0.44	0.99±0.00	0.96±0.01	-	-	-	23.75
HRINet/2	0.59±0.47	0.99±0.00	0.97±0.01	-	-	-	9.45
SiT-Small/2	0.60±0.51	0.99±0.00	0.96±0.01	-	-	-	21.70
SiM-Small/2	0.57±0.48	0.99±0.00	0.97±0.01	-	-	-	23.46
HRINet/3	<i>OOD</i>	<i>OOD</i>	<i>OOD</i>	-	-	-	9.72
SiT-Small/3	0.55±0.48	0.99±0.00	0.97±0.01	-	-	-	22.32
SiM-Small/3	0.53±0.43	0.99±0.00	0.97±0.01	-	-	-	24.08
PVTv1-Tiny	0.60±0.47	0.99±0.00	0.96±0.01	0.59±0.02	0.99±0.00	0.96±0.01	13.77
PVTv2-B1	0.57±0.47	0.99±0.00	0.97±0.01	0.58±0.03	0.99±0.00	0.97±0.01	13.61
PoolFormer-S12	0.68±0.58	0.99±0.00	0.95±0.01	0.80±0.05	0.98±0.01	0.94±0.01	12.53
MS-SiT	0.51±0.38	0.99±0.00	0.97±0.01	0.56±0.04	0.99±0.00	0.97±0.01	27.64
SurfAge-Net	0.45±0.39	0.99±0.00	0.98±0.01	0.54±0.04	0.99±0.00	0.97±0.01	14.08

F. Training Objectives

Our framework is designed for fine-grained brain age prediction. The output layer consists of 161 parallel MLP heads: 160 were assigned to predict the brain age of predefined region, and the remaining one predicted the global brain age. This design enables the model to capture both region-specific aging signatures and global aging trajectories.

Formally, for n subjects and $m = 160$ brain regions, let $\hat{y}_{i,j}$ and $y_{i,j}$ denote the global prediction and label. The region- and global-level losses are defined as:

$$L_{region} = \frac{1}{n} \sum_{i=1}^n \frac{1}{m} \sum_{j=1}^m (\hat{y}_{i,j} - y_{i,j})^2 \quad (19)$$

$$L_{global} = \frac{1}{n} \sum_{i=1}^n (\hat{y}_i - y_i)^2 \quad (20)$$

To avoid fixed assigned or manually tuned weights, we adopt an uncertainty-based multi-task learning formulation [59]. The final objective is expressed as:

$$L_{total} = \frac{1}{2\sigma_{global}^2} L_{global} + \log \sigma_{global} + \frac{1}{2\sigma_{region}^2} L_{region} + \log \sigma_{region} \quad (21)$$

where σ_{global} and σ_{region} are learnable parameters that representing task-dependent homoscedastic uncertainty of global and regional predictions, respectively.

This joint supervision encourages the model to integrate information across different scales: regional supervision promotes sensitivity to localized structural variations, while global supervision constrains the overall aging trajectory. By leveraging uncertainty-based weighting, the model adaptively balances the two objectives, yielding representations that reflect

both fine-grained regional dynamics and the integrated process of brain maturation.

G. Statistical Analysis

Model performance was evaluated using the Pearson correlation coefficient (PCC) and Spearman rank correlation coefficient (SRCC) between predicted and chronological brain age, both globally and regionally. To obtain robust estimates of correlation strength and their variability, PCC and SRCC were calculated using a bootstrap procedure with 1,000 resamples, and the mean and standard deviation were reported. To assess regional deviations between predicted and chronological brain ages, paired t-tests were conducted for each of the 160 cortical region across subjects. To characterize region-specific cortical morphological development, two-sample t-tests were performed to compare morphological measures between extremely preterm or moderate-to-late preterm groups with the term-born neonates across the 160 cortical regions, with sex and postnatal age at scan included as covariates. Multiple comparisons were corrected using the Benjamini-Hochberg false discovery rate (FDR) procedure ($q < 0.05$).

IV. RESULTS

A. Implementation Details

Our method was implemented in Python 3.8.20 using the PyTorch library, and all experiments were conducted on a single NVIDIA A100 GPU. The input data were normalized to have zero mean and unit variance. All models were trained from scratch for 1200 epochs using the AdamW optimizer $\beta_1 = 0.9$, $\beta_2 = 0.999$ with a weight decay of 1×10^{-8} and a batch size of 32. The initial learning rate was set to 5×10^{-5} , scheduled with a 20-epoch linear warmup followed by cosine decay to a minimum of 5×10^{-6} .

TABLE III
QUANTITATIVE ANALYSIS OF MODULE ABLATION EXPERIMENTS.

Model	SM	CM	CA	GF	Global MAE	Global PCC	Global SRCC	Region MAE	Region PCC	Region SRCC	Params. (M)
(a)	\times	\times	\checkmark	\times	0.69 ± 0.56	0.99 ± 0.00	0.96 ± 0.01	0.71 ± 0.07	0.99 ± 0.00	0.96 ± 0.01	6.75
(b)	\times	\checkmark	\checkmark	\times	0.54 ± 0.54	0.99 ± 0.00	0.97 ± 0.02	0.64 ± 0.03	0.99 ± 0.00	0.96 ± 0.02	7.84
(c)	\checkmark	\times	\checkmark	\times	0.54 ± 0.48	0.99 ± 0.00	0.97 ± 0.01	0.62 ± 0.01	0.99 ± 0.00	0.97 ± 0.01	11.42
(d)	\times	\times	\checkmark	\checkmark	0.64 ± 0.54	0.99 ± 0.00	0.96 ± 0.01	0.65 ± 0.02	0.99 ± 0.00	0.96 ± 0.01	8.32
(e)	\times	\checkmark	\checkmark	\checkmark	0.53 ± 0.46	0.99 ± 0.00	0.98 ± 0.01	0.62 ± 0.05	0.99 ± 0.00	0.96 ± 0.01	9.42
(f)	\checkmark	\times	\checkmark	\checkmark	0.58 ± 0.48	0.99 ± 0.00	0.96 ± 0.01	0.63 ± 0.01	0.99 ± 0.00	0.96 ± 0.01	12.99
(g)	\times	\checkmark	\times	\times	0.56 ± 0.45	0.99 ± 0.00	0.97 ± 0.01	1.12 ± 0.11	0.97 ± 0.01	0.89 ± 0.03	5.88
(h)	\checkmark	\times	\times	\times	0.57 ± 0.47	0.99 ± 0.00	0.97 ± 0.01	0.65 ± 0.06	0.99 ± 0.00	0.95 ± 0.02	9.45
(i)	\checkmark	\checkmark	\times	\times	0.54 ± 0.43	0.99 ± 0.00	0.97 ± 0.01	0.61 ± 0.01	0.99 ± 0.00	0.96 ± 0.01	10.55
(j)	\checkmark	\checkmark	\checkmark	\times	0.52 ± 0.46	0.99 ± 0.00	0.96 ± 0.01	0.60 ± 0.01	0.99 ± 0.00	0.96 ± 0.01	12.51
(k)	\checkmark	\checkmark	\checkmark	\checkmark	0.45 ± 0.39	0.99 ± 0.00	0.98 ± 0.01	0.54 ± 0.04	0.99 ± 0.00	0.97 ± 0.01	14.08

TABLE IV
QUANTITATIVE ANALYSIS OF POOLING METHODS ABLATION EXPERIMENTS.

Pooling Strategy	Global MAE	Global PCC	Global SRCC	Region MAE	Region PCC	Region SRCC
w/o SM	0.53 ± 0.46	0.99 ± 0.00	0.98 ± 0.01	0.62 ± 0.05	0.99 ± 0.00	0.96 ± 0.01
Max pool	0.51 ± 0.40	0.99 ± 0.00	0.98 ± 0.01	0.55 ± 0.02	0.99 ± 0.00	0.97 ± 0.01
Min pool	0.53 ± 0.45	0.99 ± 0.00	0.98 ± 0.01	0.55 ± 0.01	0.99 ± 0.00	0.97 ± 0.01
Mean pool	0.52 ± 0.41	0.99 ± 0.00	0.98 ± 0.01	0.58 ± 0.05	0.99 ± 0.00	0.97 ± 0.01
Weighted pool	0.51 ± 0.43	0.99 ± 0.00	0.98 ± 0.01	0.59 ± 0.02	0.99 ± 0.00	0.96 ± 0.01
Stochastic pool	0.45 ± 0.39	0.99 ± 0.00	0.98 ± 0.01	0.54 ± 0.04	0.99 ± 0.00	0.97 ± 0.01

B. Fine-Grained Infant Brain Age Prediction

To comprehensively evaluate the effectiveness of the proposed SurfAge-Net, we conducted comparative experiments on *dHCP*, benchmarking it against both GDL-based methods and recent attention- and Mamba-based architectures. The results are summarized in Table II.

We first examined global brain age prediction. Among the GDL models, PointNet++ [46] achieved the lowest MAE of 0.59, outperforming other GDL baselines whose MAEs exceeded 0.66. Attention-based methods such as HRINet [26] and SiT [16], as well as the state-space-based SiM [25] model, demonstrated superior performance over GDL models. Notably, SiM configured with an Ico-3 grid achieved the best performance among these methods, reaching an MAE of 0.53.

We then examined fine-grained prediction, in which models simultaneously estimated both global and region-level brain ages. SurfAge-Net achieved the best performance across all evaluation metrics, obtaining a whole-brain MAE of 0.45 and a region-level MAE of 0.54. Moreover, it achieved the highest PCC and SRCC, indicating stronger linear correlation and rank-order consistency with chronological age. Compared with MS-SiT [48]—the closest competitor of SurfAge-Net that attained a whole-brain MAE of 0.51 and a region-level MAE of 0.56—SurfAge-Net not only delivered higher prediction performance but also did so with approximately half the number of parameters. Other lightweight attention-based architectures, including PVTv1-Tiny [60], PVTv2-B1 [61], and PoolFormer-S12 [62], had comparable model sizes to SurfAge-Net but exhibited poorer predictive performance.

C. Ablation Experiments

1) *Effects of Different Module*: To assess the contribution of each component, we performed ablation experiments by systematically combining the four core modules: the Spatial Mixer (SM), Channel Mixer (CM), Cross-Attention (CA), and Gated Filter (GF). Configurations were denoted as models (a)-(k), shown in Table III.

Compared with the baseline model (a), models (b) and (c) exhibit consistent improvements across all evaluation metrics, demonstrating that both SM and CM effectively enhance predictive performance. Likewise, model (d) outperformed model (a) on all metrics, confirming the effectiveness of the GF module. When SM or CM was further added into the CA+GF configuration (models (e) and (f)), additional performance gains were observed, indicating that these modules provided complementary benefits.

Interestingly, model (g), which include only the CM module, performed well on global measures but relatively poor on regional metrics. This pattern, corroborated by the superior regional performance of models (b) and (i), suggested that CM primarily enhances intra-regional feature representations while lacking the ability to capture inter-regional dependencies. Finally, from models (h) to (k), we observed a progressive improvement as more modules are incorporated, with the best performance achieved when all four modules are integrated. These results highlighted the synergistic interaction among SM, CM, CA and GF, confirming the necessity of each component in achieving optimal model performance.

2) *Effects of Different Pooling Methods*: Since the SM aggregates intra-hemispheric information by pooling patch

TABLE V
QUANTITATIVE ANALYSIS OF SUBSPACE NUMBER ABLATION EXPERIMENTS.

<i>k</i>	<i>Global MAE</i>	<i>Global PCC</i>	<i>Global SRCC</i>	<i>Region MAE</i>	<i>Region PCC</i>	<i>Region SRCC</i>	<i>Params. (M)</i>
1	0.55±0.46	0.99±0.00	0.96±0.01	0.65±0.02	0.99±0.00	0.96±0.01	14.09
2	0.58±0.45	0.99±0.00	0.96±0.01	0.61±0.02	0.99±0.00	0.96±0.01	14.09
3	0.45±0.39	0.99±0.00	0.98±0.01	0.54±0.04	0.99±0.00	0.97±0.01	14.08
4	0.60±0.49	0.99±0.00	0.95±0.01	0.70±0.04	0.99±0.00	0.94±0.02	14.08

TABLE VI
QUANTITATIVE ANALYSIS OF LOSS FUNCTION ABLATION EXPERIMENTS.

<i>Loss item</i>	<i>Global MAE</i>	<i>Global PCC</i>	<i>Global SRCC</i>	<i>Region MAE</i>	<i>Region PCC</i>	<i>Region SRCC</i>	<i>Params. (M)</i>
L_{region}	-	-	-	0.78±0.05	0.98±0.01	0.93±0.02	14.08
L_{global}	0.79±0.84	0.98±0.01	0.91±0.03	-	-	-	14.02
$L_{global}+L_{region}$	0.52±0.41	0.99±0.00	0.97±0.01	0.60±0.02	0.99±0.00	0.97±0.01	14.08
L_{total}	0.45±0.39	0.99±0.00	0.98±0.01	0.54±0.04	0.99±0.00	0.97±0.01	14.08

features into a global representation, the choice of pooling strategy critically determines the quality of this representation. We compared several pooling methods, including max pooling, min pooling, mean pooling, weighted pooling and stochastic pooling, along with a variant where the SM was entirely removed.

According to Table IV, the results showed that stochastic pooling achieved the best overall performance, whereas removing the SM led to the worst outcomes. This finding confirmed the importance of explicitly modeling intra-hemispheric interactions for accurate brain age prediction. Among the deterministic pooling methods, max pooling performed relatively better, suggesting that salient features played an important role in capturing hemispheric characteristics. In contrast, min pooling yielded the weakest result, likely due to its bias toward less informative features. Weighted and mean pooling exhibited moderate performance, but both remained inferior to stochastic pooling. These findings indicated that stochastic pooling is particularly well-suited for constructing robust hemispheric representations. From a biological perspective, this aligns with the fact that neuronal communication is inherently probabilistic rather than strictly deterministic [63], [64]. The stochastic mechanism may thus better capture the uncertainty and variability underlying intra-hemispheric information integration in the developing brain.

3) *Effects of Different Number of Subspace*: The CM enhanced patch-level representations by uniformly splitting each feature vector into k subspaces, analogous to the multi-head design in attention mechanisms. This partitioning enables the model to learn complementary sub-representations from different feature subsets. To access the impact of this design, we evaluated different settings of $k \in \{1, 2, 3, 4\}$, shown in Table V.

The results revealed that dividing features into three subspaces yielded the best overall performance, while four subspaces produced the worst outcomes. Configurations with one or two subspaces showed intermediate performance. These

findings suggested a trade-off between representational diversity and per-subspace capacity. Specifically, increasing the number of subspaces enriches diversity by promoting disentangled learning, but simultaneously reduces the dimensionality of each subspace, potentially weakening its modeling capability. In our experiments, employing only one or two subspaces limited the ability of model to disentangle heterogeneous information, thereby constraining its expressive power. In contrast, using four subspaces might excessively fragmented the feature space, leading to unstable optimization and degraded performance. The three-subspace configuration appeared to achieve an optimal balance, offering sufficient diversity to capture complementary aging-related patterns while maintaining adequate feature dimensionality for effective representation learning.

4) *Effects of Different Designs of Loss*: To evaluate the impact of supervision strategies, we compared four loss designs: (1) using only the mean regional MSE, (2) using only the global MSE, (3) directly summing the two losses, and (4) combining both losses with uncertainty-based learnable weights.

In Table VI, the results showed that using either regional or global supervision alone led to suboptimal performance, with both single-loss variants yielding comparable results. Incorporating both losses (design 3) yielded a noticeable improvement, demonstrating that joint supervision enabled the model to capture complementary information from fine-grained regional patterns and overall brain-level developmental trajectories. The best performance was achieved by the uncertainty-weighted combination (design 4), consistently outperforming all other configurations across all evaluation metrics, which highlighted the importance of adaptive loss balancing, as the relative contributions of local and global information may vary throughout training. By allowing the model to dynamically adjust this balance, the optimization process became more flexible and better aligned with the intrinsic multi-scale structure of brain development.

TABLE VII
GENERALIZATION VALIDATION ON IMAGES OF TERM-BORN NEONATES IN GSMCH.

Methods	Global MAE	Global PCC	Global SRCC	Region MAE	Region PCC	Region SRCC
PVTv1-Tiny	1.18±0.70	0.67±0.17	0.59±0.28	1.19±0.11	0.66±0.17	0.69±0.21
PVTv2-B1	1.59±0.80	0.73±0.17	0.82±0.17	1.51±0.17	0.71±0.17	0.79±0.16
PoolFormer-S12	1.26±0.94	0.43±0.30	0.38±0.34	2.08±0.98	0.25±0.27	0.25±0.30
MS-SiT	1.82±0.81	0.74±0.09	0.83±0.12	1.85±0.14	0.62±0.14	0.66±0.19
SurfAge-Net	0.63±0.51	0.83±0.07	0.62±0.20	0.92±0.20	0.75±0.11	0.78±0.14

TABLE VIII
GENERALIZATION VALIDATION ON FETAL IMAGES IN LZUSH.

Methods	Global MAE	Global PCC	Global SRCC	Region MAE	Region PCC	Region SRCC
PVTv1-Tiny	1.28±1.27	0.89±0.04	0.85±0.06	1.27±0.05	0.88±0.04	0.85±0.06
PVTv2-B1	1.10±1.16	0.88±0.05	0.83±0.07	1.13±0.04	0.88±0.05	0.83±0.07
PoolFormer-S12	1.77±1.01	0.96±0.01	0.96±0.02	2.58±0.59	0.76±0.07	0.76±0.08
MS-SiT	1.26±1.15	0.90±0.04	0.86±0.06	1.36±0.09	0.88±0.04	0.84±0.06
SurfAge-Net	1.02±0.66	0.96±0.01	0.96±0.01	1.10±0.11	0.94±0.01	0.94±0.03

D. Generalization Validation on Normative Cohort

To assess the generalizability of different models, we evaluated their performance on images of term newborns in *GSMCH* and fetuses in *LZUSH*, respectively, as summarized in Table VII and Table VIII. Although all models exhibited degradation across all metrics when transferred to the independent cohorts, *SurfAge-Net* consistently achieved the best performance, attaining the best generalization in both datasets. Notably, *MS-SiT*, which performed comparably to *SurfAge-Net* on *dHCP*, showed a marked decline under distributional shifts, suggesting limited robustness to variations in population characteristics.

Interestingly, distinct patterns were observed between the two normative subsets. On term-born neonates in *GSMCH*, lower MAE was accompanied by reduced PCC and SRCC. This likely reflected the very small sample size (16 infants), where random fluctuations can disproportionately affect correlation measures, resulting in small absolute errors but less stable rank ordering of predicted ages. Conversely, on *LZUSH*, the MAE was higher, but both PCC and SRCC improved, likely due to the larger sample size (49 fetuses) could provide more reliable ordering and greater stability in correlations estimates. These results demonstrated that *SurfAge-Net* maintained superior generalizability across cohorts, even under substantial domain shifts, and that performance variations across subsets may reflect differences in sample size and label granularity rather than deficiencies in model robustness.

E. Analysis on Atypical Developmental Infants

Fig 7 illustrates both regional and global deviations in cortical maturation across term-born neonates and three atypical developmental cohorts. For the term-born neonates, cortical development appeared largely typical, with minimal regional deviations in cortical maturation (Panels A-B) and no regions exhibiting significant developmental delays or accelerations.

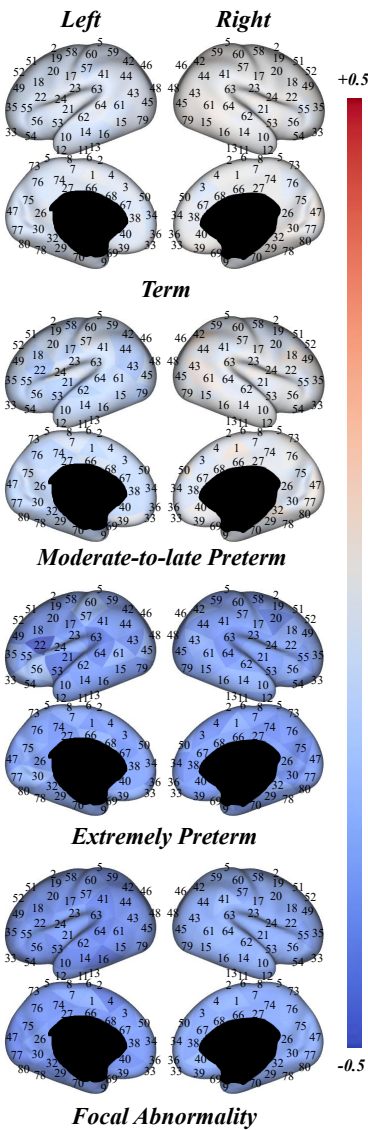
The global brain age did not differ significantly from chronological age.

For the moderate-to-late preterm group, cortical development was predominant delayed, particularly across the left hemisphere, which consistently lagged behind chronological age (Panels A-B). In contrast, several right-hemisphere regions, such as Superior Frontal Gyrus (region 1), Caudal Middle Frontal (region 18), and Parahippocampal (region 32), showed slight but nonsignificant overdevelopment. Marked regional developmental heterogeneity was evident (Panel B): while regions in the right hemisphere approximated normative age, several left-hemisphere regions exhibited delays of up to ~0.2 weeks. Except for the left hemisphere sensorimotor and superior parietal regions (regions 2, 4-8), the lateral temporal cortex (regions 11, 12), central sensorimotor strip (regions 41, 57, 60, 61, 63), insular cortex (regions 16, 19-21, 23, 24), and the frontoparietal cortex (regions 45, 46, 49, 50), most cortical regions showed significantly lower predicted brain age than chronological age, indicating widespread cortical maturation delay. The global brain age was also significantly lower than chronological age (Panel C).

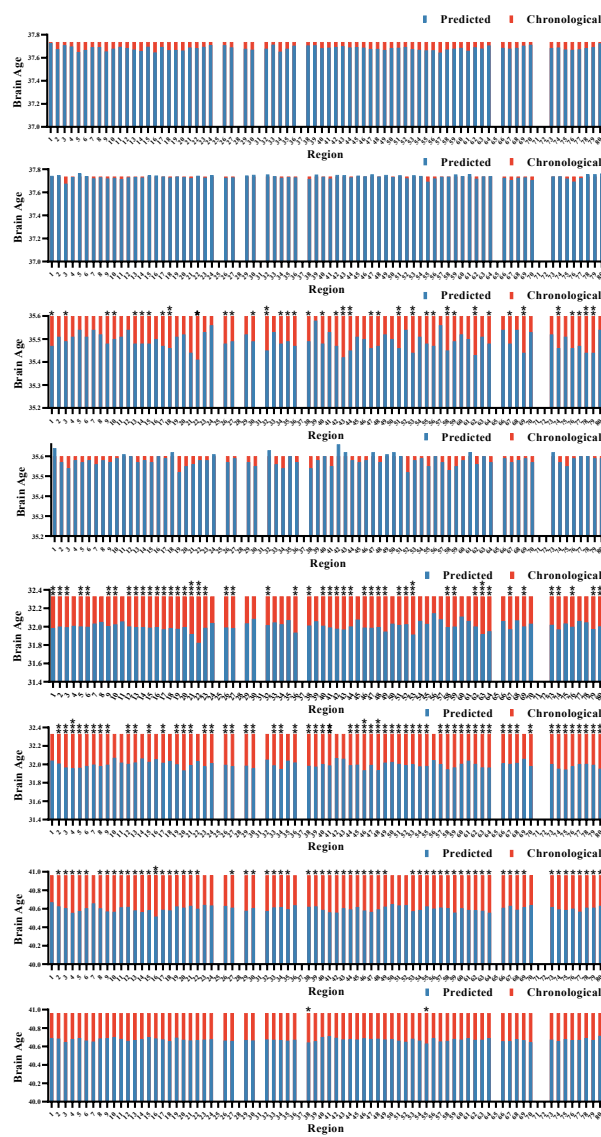
For the extremely preterm group, more pronounced cortical delays were observed across both hemispheres (panel A), with an average delay of approximately 0.4 weeks (panel B). Compared with the moderate-to-late preterm group, a larger number of regions exhibited significant developmental delays, accompanied by a more evident reduction in global brain age ($p < 0.01$, panel C).

Similar to the two preterm cohorts, neonates with focal brain abnormality showed reduced brain age both globally and regionally (panel A-C), with an overall severity intermediate between the moderate-to-late and extremely preterm groups (panel B). In the left hemisphere, nearly all regions, except the sensorimotor regions (regions 23, 24, 26) and the frontal cortex (regions 50-52), showed significant developmental delays. In

A. Visualization of predicted regional age



B. Region Difference



C. Global Difference

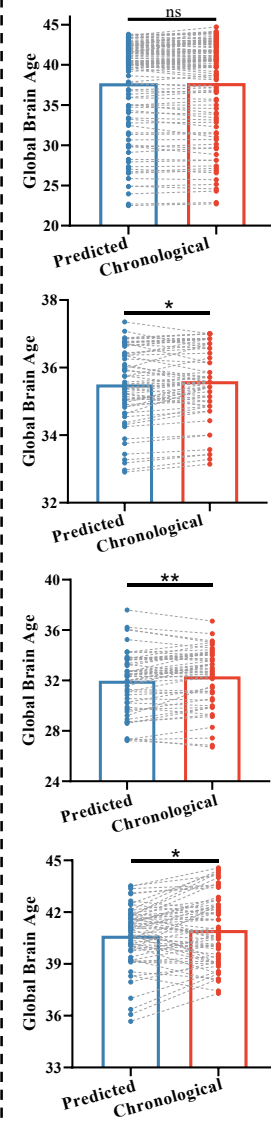


Fig. 7. Regional and global brain developmental deviations in atypical developmental populations. (A) Visualization of predicted regional ages. Cortical surface maps intuitively illustrate the developmental status of each brain region, with regional indices annotated. Colors represent the deviation between predicted and chronological ages: positive values (e.g., +0.5) indicate accelerated development (0.5 weeks ahead), whereas negative values (e.g., -0.5) indicate delayed development (0.5 weeks behind). (B) Bar plots of regional differences. Comparisons between predicted and chronological ages across 80 cortical regions for the left and right hemispheres, respectively. Each bar corresponds to one region, enabling assessment of localized developmental deviations. $*p < 0.05$, $**p < 0.01$, $***p < 0.001$ (paired t-test, FDR-corrected). (C) Global brain age differences. Paired-sample t-tests compare predicted global brain age with chronological age, highlighting overall developmental deviations in the atypical developmental cohort. Paired samples t-test: ns represents no significance, $*p < 0.05$, $**p < 0.01$, $***p < 0.001$ (paired-test).

the right hemisphere, only the Superior Frontal Gyrus (region 38) and Pars Triangularis (region 55) exhibited comparable alterations. These findings highlighted the clinical relevance of fine-grained brain age prediction. Infants born at earlier gestational ages or presenting with focal brain abnormalities exhibited measurable developmental delays, suggesting the potential utility of SurfAge-Net-derived brain age as a promising biomarker for early risk stratification and personalized intervention planning to mitigate long-term neurodevelopmental deficits.

F. External Validation on Atypical Developmental Infants

To further assess the external validity of SurfAge-Net, we examined two atypical developmental populations from the *GSMCH* datasets. Both groups showed significantly decreased predicted global and regional ages relative to chronological age (Fig. 8), consistent with the results observed in the *dHCP* datasets. For the moderate-to-late preterm group, widespread cortical developmental delays were found, with the left hemisphere exhibiting substantially greater delays than the right (approximately 0.7 weeks on average, panel A-B). The average delay was about ~ 1 week in the left hemisphere and ~ 0.3

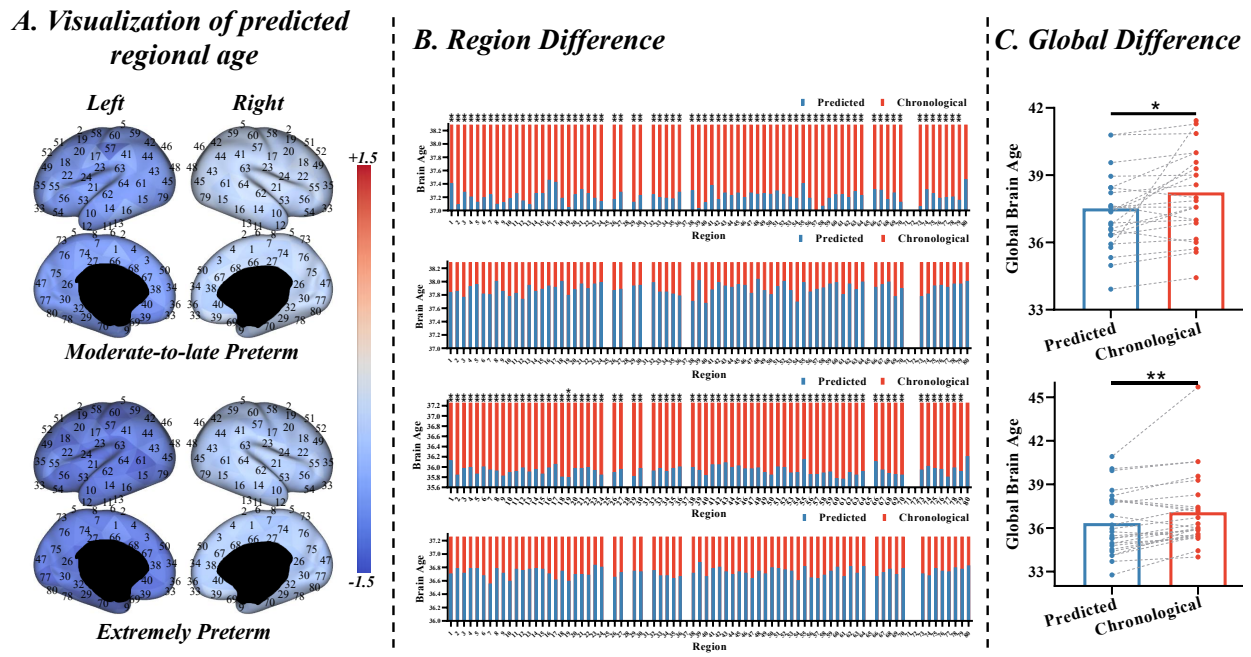


Fig. 8. Regional and global brain developmental deviations in abnormal developmental populations from external datasets. (A) Visualization of predicted regional ages. Colors represent the deviation between predicted and chronological ages: positive values (e.g., +1.5) indicate accelerated development (1.5 weeks ahead), whereas negative values (e.g., -1.5) indicate delayed development (1.5 weeks behind). (B) Bar plots of regional differences. (C) Global brain age differences.

weeks in the right (panel B). Marked regional heterogeneity was also observed, as almost all regions in the left hemisphere exhibited pronounced maturation delays. The global brain age was significantly lower than chronological age ($p < 0.05$). For the extremely preterm group in *GSMCH*, similar spatial and global patterns were observed, but with more pronounced severity (panels A-C). The left hemisphere exhibited comparable levels of delay, with the Precentral Gyrus (region 19) showing the most pronounced deficit.

G. Regional Deviation of Local Morphological Indicators

To characterize region-specific cortical morphological development during the perinatal period, we examined how mean curvature, sulcal depth, and thickness vary across different cortical regions in preterm infants relative to term controls, and further investigated their associations with regional brain age gap. As observed in Fig. 9, analysis of regional morphological deviations revealed distinct and feature-specific alteration patterns in preterm infants relative to term controls. Notably, sulcal depth and cortical thickness in the prefrontal and limbic cortices were significantly reduced in preterm infants, with the magnitude of reduction increasing with decreasing gestational age, indicating a dose-dependent effect of prematurity. In contrast, curvature exhibited a divergent pattern: prefrontal and temporo-parietal junction regions showed significantly increased curvature in extremely preterm infants, accompanied by elevated sulcal depth in parietal and medial cortical regions. Importantly, these curvature and sulcal depth increases were largely absent in the moderate-to-late preterm group, suggesting that such alterations are specific to more severe prematurity and are not captured by moderate deviations in

gestational age. Notably, although the brain-age gap increased globally from moderate-to-late to extremely preterm infants, local cortical morphological changes did not converge toward a uniform direction. This inconsistency likely reflects the non-linear and region-specific nature of perinatal cortical development, during which measures such as curvature and thickness may follow inverted U-shaped or otherwise non-monotonic trajectories around the term-equivalent window [23]. As a result, elevated or attenuated local morphological measures in extremely preterm infants may indicate altered developmental timing rather than a simple linear relationship with global brain-age delay.

V. DISCUSSION

In this study, we introduced a novel patch-level brain age prediction framework, termed SurfAge-Net, which enables precise and region-specific assessment of cortical maturation in infancy. SurfAge-Net achieved substantial performance gains over existing methods in both global and regional brain-age prediction and demonstrated strong generalizability across multiple independent cohorts. By capturing fine-grained variations in cortical development, SurfAge-Net revealed complex and heterogeneous developmental patterns throughout the cortex that are often masked by coarser-scale approaches. Importantly, the model successfully identified subtle developmental delays in atypical neonate populations, including preterm and focal abnormality groups, highlighting its potential as a sensitive biomarker for early neurodevelopmental risks stratification.

Unlike conventional whole-brain models that yield only a single global brain age, SurfAge-Net could delineate heterogeneous maturation degree within an individual brain, providing

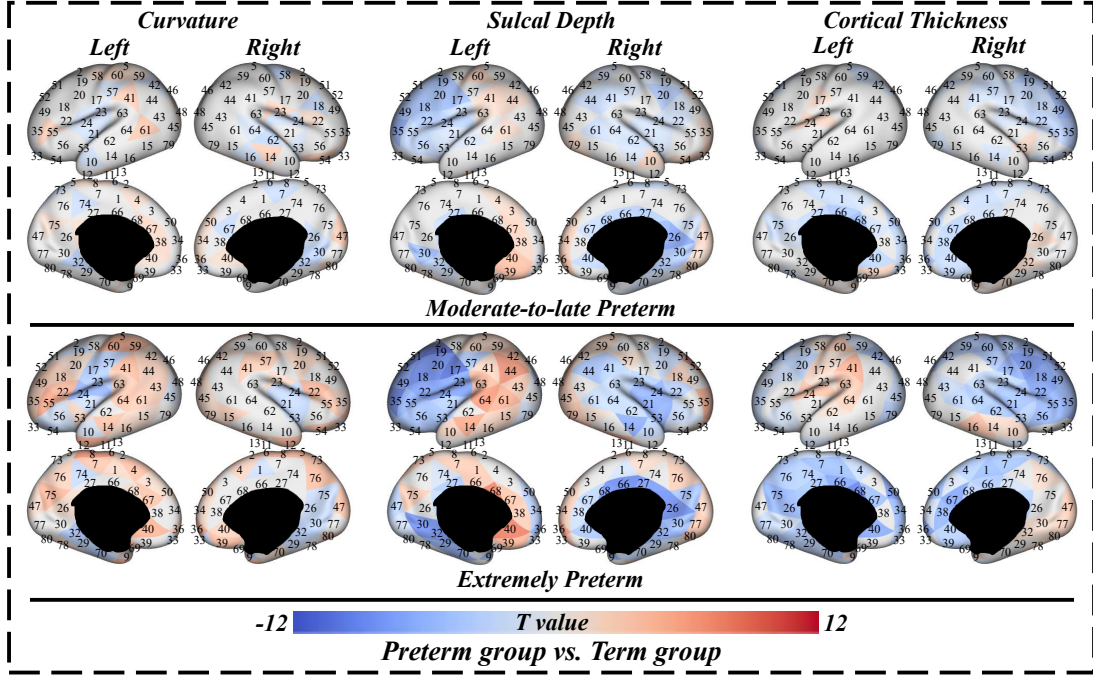


Fig. 9. Regional differences in cortical morphology between preterm and term neonates. Multiple comparisons were corrected by the FDR method, and brain regions with $q < 0.05$ were visualized.

new insight into the dynamic and regionally asynchronous nature of early brain development. The fine-grained, patch-level framework further enables precise localization of developmental abnormalities at the cortical region level, identifying specific cortical regions that deviate from normative trajectories. This spatial resolution offers critical clinical value, revealing which cortical areas are most susceptible to atypical development—such as the sensorimotor, temporal, and frontoparietal cortices that are commonly affected in preterm infants [65], [66]. In this study, this spatially resolved modeling revealed marked heterogeneity in cortical maturation in preterm infants, with accelerated development in prefrontal cortex and postcentral gyrus and delayed maturation in most of the high-order cortices, consistent with the hierarchical pattern of cortical development observed in previous studies [9], [65], [67], in which primary sensorimotor and visual areas mature earlier than high-order association areas. Such localization enhances both clinical interpretability and practicability of brain age modeling, facilitating early diagnosis and individualized intervention strategies tailored to specific cortical vulnerabilities.

The human brain is organized as a complex, interconnected network rather than isolated regions. Morphometric similarity network studies have shown that brain regions with similar developmental trajectories tend to form tightly coupled networks, reflecting coordinated maturation across the cortex [10], [68], [69]. Therefore, predicting the developmental age of a single cortical patch necessitates integrating information not only from the target patch but also from anatomically and functionally related regions. In addition, brain asymmetry is a fundamental characteristic of early brain development, manifested as structural lateralization, differential growth rates,

and asymmetric gene expression patterns between bilateral hemispheres [70], [71], [72]. SurfAge-Net embodies these neurodevelopmental principles by explicitly modeling both intra-hemispheric dependencies and inter-hemispheric interactions, while accounting for hemispheric asymmetry in maturation. Within each hemisphere, the Spatial Mixer aggregates contextual information from related patches to capture coordinated morphological patterns, and the Channel Mixer adaptively reweights feature channels according to their contribution to brain age prediction, thereby enhancing informative signals while suppressing redundant or noisy signals. To model contralateral influences, the Dynamic Lateralization-Aware Attention mechanism selectively integrates information from the opposite hemisphere, regulated by gating filters that filter out irrelevant inputs. The improved performance of SurfAge-Net demonstrates that modeling these complex spatial relationships (i.e., ipsilateral heterogeneity and contralateral connectivity) is essential for accurately characterizing fine-grained, region-specific developmental trajectories. This also enables the model to reveal subtle, spatially organized maturational dynamics that traditional whole-brain methods often overlook. Moreover, SurfAge-Net consistently predicts younger brain ages in the left hemisphere compared to the right across multiple datasets, which is in line with established lateralization patterns in early brain development [73]. This asymmetry likely corresponds to differential maturation rates and emerging functional specializations between hemispheres [74], [75].

Our results provide strong evidence supporting the clinical interpretability of SurfAge-Net by demonstrating findings closely aligned with previous neuroimaging studies linking prematurity and focal lesions to disrupted cortical growth and

delayed structural maturation [9], [76]. The predicted brain age exhibits graded decline from term-born neonates to moderate-to-late preterm, and further to extremely preterm infants, reflecting a continuum of neurodevelopmental impairment that mirrors clinical observations of increasing gestational risk severity [77], [78]. This progressive decrease in predicted brain age not only validates clinical reliability of SurfAge-Net, but also demonstrates its sensitivity to varying degrees of atypical developmental conditions. Furthermore, the spatial patterns of cortical maturation delays identified by SurfAge-Net correspond with established findings of regionally heterogeneous brain development in early infancy [9], [70]. Specifically, the model reveals pronounced delays in regions such as the prefrontal, lateral temporal, and sensorimotor cortices in extremely premature infants, consistent with diffuse cortical immaturity and region-specific vulnerability reported in the previous literature [65], [79], [80]. The observed gradient—from relatively preserved maturation in moderate-to-late preterm infants to more widespread delays in extremely preterm cases—further confirms SurfAge-Net’s ability to detect subtle regional variations during cortical development. These results indicate that SurfAge-Net not only reflects global developmental trends but also precisely maps region-specific alterations, thereby providing a biologically plausible and clinically interpretable framework for characterizing atypical cortical maturation in the developing brain.

Despite the promising results, there are several limitations that should be acknowledged. First, the sample size across the three datasets remain relatively limited, necessitating future validation on larger and diverse cohorts to ensure the generalizability and robustness of the proposed paradigm. Second, although our patch-level brain age prediction provides finer resolution than whole-brain prediction approaches, it may still be relatively coarse. Future studies could explore vertex-level or even higher-resolution predictions to achieve more precise characterization of cortical development. Third, while our focus was primarily on cortical features, other clinical variables such as genetic factors, perinatal complications, and environmental influences, were not incorporated. Integrating these multimodal data could further enhance prediction accuracy and clinical interpretability. Lastly, the present work focuses exclusively on early brain development; expanding this approach to other conditions like childhood development and aging could enable a more comprehensive evaluation of brain health across the lifespan.

VI. CONCLUSION

We introduce SurfAge-Net, the first fine-grained, patch-level brain age prediction paradigm that achieves state-of-the-art performance across three datasets, with a global MAE of 0.54 and a regional MAE of 0.45. SurfAge-Net facilitates precise and clinically interpretable mapping of atypical cortical development in clinical populations, including moderate-to-late preterm, extremely preterm, and focal abnormality infants. By providing a sensitive, region-specific insights into neurodevelopmental deviations, SurfAge-Net offers a powerful tool for early detection, risk stratification, and personalized intervention in pediatric neurological care.

REFERENCES

- [1] G. Dehaene-Lambertz and E. S. Spelke, “The infancy of the human brain,” *Neuron*, vol. 88, no. 1, pp. 93–109, 2015.
- [2] S. Wilson, M. Pietsch, L. Cordero-Grande, A. N. Price, J. Hutter, J. Xiao, L. McCabe, M. A. Rutherford, E. J. Hughes, S. J. Counsell *et al.*, “Development of human white matter pathways in utero over the second and third trimester,” *Proceedings of the National Academy of Sciences*, vol. 118, no. 20, p. e2023598118, 2021.
- [3] K. Franke, E. Luders, A. May, M. Wilke, and C. Gaser, “Brain maturation: predicting individual brainage in children and adolescents using structural mri,” *Neuroimage*, vol. 63, no. 3, pp. 1305–1312, 2012.
- [4] L. B. Whitmore, S. J. Weston, and K. L. Mills, “Brainage as a measure of maturation during early adolescence,” *Imaging Neuroscience*, vol. 1, pp. 1–21, 2023.
- [5] D. J. Licht, D. M. Shera, R. R. Clancy, G. Wernovsky, L. M. Montenegro, S. C. Nicolson, R. A. Zimmerman, T. L. Spray, J. W. Gaynor, and A. Vossough, “Brain maturation is delayed in infants with complex congenital heart defects,” *The Journal of thoracic and cardiovascular surgery*, vol. 137, no. 3, pp. 529–537, 2009.
- [6] H. C. Hazlett, H. Gu, B. C. Munsell, S. H. Kim, M. Styner, J. J. Wolff, J. T. Elison, M. R. Swanson, H. Zhu, K. N. Botteron *et al.*, “Early brain development in infants at high risk for autism spectrum disorder,” *Nature*, vol. 542, no. 7641, pp. 348–351, 2017.
- [7] S. He, P. E. Grant, and Y. Ou, “Global-local transformer for brain age estimation,” *IEEE transactions on medical imaging*, vol. 41, no. 1, pp. 213–224, 2021.
- [8] W. Zheng, X. Wang, T. Liu, B. Hu, and D. Wu, “Preterm-birth alters the development of nodal clustering and neural connection pattern in brain structural network at term-equivalent age,” *Human Brain Mapping*, vol. 44, no. 16, pp. 5372–5386, 2023.
- [9] R. Dimitrova, M. Pietsch, J. Ciarrusta, S. P. Fitzgibbon, L. Z. Williams, D. Christiaens, L. Cordero-Grande, D. Batalle, A. Makropoulos, A. Schuh *et al.*, “Preterm birth alters the development of cortical microstructure and morphology at term-equivalent age,” *NeuroImage*, vol. 243, p. 118488, 2021.
- [10] Y. Wang, D. Zhu, L. Zhao, X. Wang, Z. Zhang, B. Hu, D. Wu, and W. Zheng, “Profiling cortical morphometric similarity in perinatal brains: insights from development, sex difference, and inter-individual variation,” *NeuroImage*, vol. 295, p. 120660, 2024.
- [11] P. Shaw, N. J. Kabani, J. P. Lerch, K. Eckstrand, R. Lenroot, N. Gogtay, D. Greenstein, L. Clasen, A. Evans, J. L. Rapoport *et al.*, “Neurodevelopmental trajectories of the human cerebral cortex,” *Journal of neuroscience*, vol. 28, no. 14, pp. 3586–3594, 2008.
- [12] Y. Huang, Z. Wu, F. Wang, D. Hu, T. Li, L. Guo, L. Wang, W. Lin, and G. Li, “Mapping developmental regionalization and patterns of cortical surface area from 29 post-menstrual weeks to 2 years of age,” *Proceedings of the National Academy of Sciences*, vol. 119, no. 33, p. e2121748119, 2022.
- [13] W. Zheng, L. Zhao, Z. Zhao, T. Liu, B. Hu, and D. Wu, “Spatiotemporal developmental gradient of thalamic morphology, microstructure, and connectivity from the third trimester to early infancy,” *Journal of Neuroscience*, vol. 43, no. 4, pp. 559–570, 2023.
- [14] M. E. Thomason, “Development of brain networks in utero: relevance for common neural disorders,” *Biological psychiatry*, vol. 88, no. 1, pp. 40–50, 2020.
- [15] X. Wu, C. Xie, F. Cheng, Z. Li, R. Li, D. Xu, H. Kim, J. Zhang, H. Liu, and M. Liu, “Comparative evaluation of interpretation methods in surface-based age prediction for neonates,” *NeuroImage*, vol. 300, p. 120861, 2024.
- [16] S. Dahan, A. Fawaz, L. Z. Williams, C. Yang, T. S. Coalson, M. F. Glasser, A. D. Edwards, D. Rueckert, and E. C. Robinson, “Surface vision transformers: Attention-based modelling applied to cortical analysis,” in *International Conference on Medical Imaging with Deep Learning*. PMLR, 2022, pp. 282–303.
- [17] Z. Li, J. Zhang, Y. Zeng, J. Lin, D. Zhang, J. Zhang, D. Xu, H. Kim, B. Liu, and M. Liu, “Surfgnn: A robust surface-based prediction model with interpretability for coactivation maps of spatial and cortical features,” *Medical Image Analysis*, p. 103793, 2025.
- [18] J. H. Cole, R. P. Poudel, D. Tsagkrasoulis, M. W. Caan, C. Steves, T. D. Spector, and G. Montana, “Predicting brain age with deep learning from raw imaging data results in a reliable and heritable biomarker,” *NeuroImage*, vol. 163, pp. 115–124, 2017.
- [19] C. Dartora, A. Marseglia, G. Mårtensson, G. Rukh, J. Dang, J.-S. Muehlboeck, L.-O. Wahlund, R. Moreno, J. Barroso, D. Ferreira *et al.*, “A deep learning model for brain age prediction using minimally

preprocessed t1w images as input," *Frontiers in Aging Neuroscience*, vol. 15, p. 1303036, 2024.

[20] G. Spalletta, F. Piras, T. Gili *et al.*, *Brain morphometry*. Springer, 2018.

[21] Y. Wang, Y. Zhang, W. Zheng, X. Liu, Z. Zhao, S. Li, N. Chen, L. Yang, L. Fang, Z. Yao *et al.*, "Age-related differences of cortical topology across the adult lifespan: Evidence from a multisite mri study with 1427 individuals," *Journal of Magnetic Resonance Imaging*, vol. 57, no. 2, pp. 434–443, 2023.

[22] R. A. Bethlehem, J. Seidlitz, S. R. White, J. W. Vogel, K. M. Anderson, C. Adamson, S. Adler, G. S. Alexopoulos, E. Anagnostou, A. Areces-Gonzalez *et al.*, "Brain charts for the human lifespan," *Nature*, vol. 604, no. 7906, pp. 525–533, 2022.

[23] X. Xu, C. Sun, J. Sun, W. Shi, Y. Shen, R. Zhao, W. Luo, M. Li, G. Wang, and D. Wu, "Spatiotemporal atlas of the fetal brain depicts cortical developmental gradient," *Journal of Neuroscience*, vol. 42, no. 50, pp. 9435–9449, 2022.

[24] Y. Sheng, Y. Wang, X. Wang, Z. Zhang, D. Zhu, and W. Zheng, "No sex difference in maturation of brain morphology during the perinatal period," *Brain Structure and Function*, vol. 229, no. 8, pp. 1979–1994, 2024.

[25] R. He, W. Zheng, L. Zhao, Y. Wang, D. Zhu, D. Wu, and B. Hu, "Surface vision mamba: Leveraging bidirectional state space model for efficient spherical manifold representation," in *International Conference on Medical Image Computing and Computer-Assisted Intervention*. Springer, 2025, pp. 599–608.

[26] L. Zhao, D. Zhu, X. Wang, X. Liu, T. Li, B. Wang, Z. Yao, W. Zheng, and B. Hu, "An attention-based hemispheric relation inference network for perinatal brain age prediction," *IEEE Journal of Biomedical and Health Informatics*, vol. 28, no. 8, pp. 4483–4493, 2024.

[27] W. Zheng, T. Eilam-Stock, T. Wu, A. Spagna, C. Chen, B. Hu, and J. Fan, "Multi-feature based network revealing the structural abnormalities in autism spectrum disorder," *IEEE Transactions on Affective Computing*, vol. 12, no. 3, pp. 732–742, 2019.

[28] O. Sporns, D. R. Chialvo, M. Kaiser, and C. C. Hilgetag, "Organization, development and function of complex brain networks," *Trends in cognitive sciences*, vol. 8, no. 9, pp. 418–425, 2004.

[29] Y. Chung, J. Addington, C. E. Bearden, K. Cadenhead, B. Cornblatt, D. H. Mathalon, T. McGlashan, D. Perkins, L. J. Seidman, M. Tsuang *et al.*, "Use of machine learning to determine deviance in neuroanatomical maturity associated with future psychosis in youths at clinically high risk," *JAMA psychiatry*, vol. 75, no. 9, pp. 960–968, 2018.

[30] B. G. Becker, T. Klein, C. Wachinger, A. D. N. Initiative *et al.*, "Gaussian process uncertainty in age estimation as a measure of brain abnormality," *NeuroImage*, vol. 175, pp. 246–258, 2018.

[31] D. Hu, Z. Wu, W. Lin, G. Li, and D. Shen, "Hierarchical rough-to-fine model for infant age prediction based on cortical features," *IEEE journal of biomedical and health informatics*, vol. 24, no. 1, pp. 214–225, 2019.

[32] I. Beheshti, N. Maikusa, and H. Matsuda, "The accuracy of t1-weighted voxel-wise and region-wise metrics for brain age estimation," *Computer Methods and Programs in Biomedicine*, vol. 214, p. 106585, 2022.

[33] X. Liu, I. Beheshti, W. Zheng, Y. Li, S. Li, Z. Zhao, Z. Yao, and B. Hu, "Brain age estimation using multi-feature-based networks," *Computers in Biology and Medicine*, vol. 143, p. 105285, 2022.

[34] T.-W. Huang, H.-T. Chen, R. Fujimoto, K. Ito, K. Wu, K. Sato, Y. Taki, H. Fukuda, and T. Aoki, "Age estimation from brain mri images using deep learning," in *2017 IEEE 14th International Symposium on Biomedical Imaging (ISBI 2017)*. IEEE, 2017, pp. 849–852.

[35] M. Ueda, K. Ito, K. Wu, K. Sato, Y. Taki, H. Fukuda, and T. Aoki, "An age estimation method using 3d-cnn from brain mri images," in *2019 IEEE 16th international symposium on biomedical imaging (ISBI 2019)*. IEEE, 2019, pp. 380–383.

[36] B. A. Jónsson, G. Björnsdóttir, T. E. Thorgerisson, L. M. Ellingsen, G. B. Walters, D. F. Gudbjartsson, H. Stefansson, K. Stefansson, and M. O. Ulfarsson, "Brain age prediction using deep learning uncovers associated sequence variants," *Nature communications*, vol. 10, no. 1, p. 5409, 2019.

[37] X. Feng, Z. C. Lipton, J. Yang, S. A. Small, F. A. Provenzano, A. D. N. Initiative, F. L. D. N. Initiative *et al.*, "Estimating brain age based on a uniform healthy population with deep learning and structural magnetic resonance imaging," *Neurobiology of aging*, vol. 91, pp. 15–25, 2020.

[38] V. M. Bashyam, G. Erus, J. Doshi, M. Habes, I. M. Nasrallah, M. Truelove-Hill, D. Srinivasan, L. Mamourian, R. Pomponio, Y. Fan *et al.*, "Mri signatures of brain age and disease over the lifespan based on a deep brain network and 14 468 individuals worldwide," *Brain*, vol. 143, no. 7, pp. 2312–2324, 2020.

[39] A. Fawaz, L. Z. Williams, A. Alansary, C. Bass, K. Gopinath, M. da Silva, S. Dahan, C. Adamson, B. Alexander, D. Thompson *et al.*, "Benchmarking geometric deep learning for cortical segmentation and neurodevelopmental phenotype prediction," *bioRxiv*, pp. 2021–12, 2021.

[40] V. Vosylius, A. Wang, C. Waters, A. Zakharov, F. Ward, L. Le Folgoe, J. Cupitt, A. Makropoulos, A. Schuh, D. Rueckert *et al.*, "Geometric deep learning for post-menstrual age prediction based on the neonatal white matter cortical surface," in *International Workshop on Uncertainty for Safe Utilization of Machine Learning in Medical Imaging*. Springer, 2020, pp. 174–186.

[41] F. Monti, D. Boscaini, J. Masci, E. Rodola, J. Svoboda, and M. M. Bronstein, "Geometric deep learning on graphs and manifolds using mixture model cnns," in *Proceedings of the IEEE conference on computer vision and pattern recognition*, 2017, pp. 5115–5124.

[42] T. S. Cohen, M. Geiger, J. Köhler, and M. Welling, "Spherical cnns," *arXiv preprint arXiv:1801.10130*, 2018.

[43] M. Defferrard, X. Bresson, and P. Vandergheynst, "Convolutional neural networks on graphs with fast localized spectral filtering," *Advances in neural information processing systems*, vol. 29, 2016.

[44] T. Kipf, "Semi-supervised classification with graph convolutional networks," *arXiv preprint arXiv:1609.02907*, 2016.

[45] F. Zhao, S. Xia, Z. Wu, D. Duan, L. Wang, W. Lin, J. H. Gilmore, D. Shen, and G. Li, "Spherical u-net on cortical surfaces: methods and applications," in *International Conference on Information Processing in Medical Imaging*. Springer, 2019, pp. 855–866.

[46] C. R. Qi, L. Yi, H. Su, and L. J. Guibas, "Pointnet++: Deep hierarchical feature learning on point sets in a metric space," *Advances in neural information processing systems*, vol. 30, 2017.

[47] H. Zhao, H. Cai, and M. Liu, "Transformer based multi-modal mri fusion for prediction of post-menstrual age and neonatal brain development analysis," *Medical Image Analysis*, vol. 94, p. 103140, 2024.

[48] S. Dahan, L. Z. Williams, D. Rueckert, and E. C. Robinson, "The multiscale surface vision transformer," *ArXiv*, pp. arXiv–2303, 2024.

[49] A. Gu and T. Dao, "Mamba: Linear-time sequence modeling with selective state spaces," in *First conference on language modeling*, 2024.

[50] A. Cherubini, M. E. Caliguri, P. Péran, U. Sabatini, C. Cosentino, and F. Amato, "Importance of multimodal mri in characterizing brain tissue and its potential application for individual age prediction," *IEEE journal of biomedical and health informatics*, vol. 20, no. 5, pp. 1232–1239, 2016.

[51] T. Kaufmann, D. van der Meer, N. T. Doan, E. Schwarz, M. J. Lund, I. Agartz, D. Alnæs, D. M. Barch, R. Baur-Streubel, A. Bertolino *et al.*, "Common brain disorders are associated with heritable patterns of apparent aging of the brain," *Nature neuroscience*, vol. 22, no. 10, pp. 1617–1623, 2019.

[52] P. Hof, P. Giannakopoulos, and C. Bouras, "The neuropathological changes associated with normal brain aging," *Histology and histopathology*, 1996.

[53] N. Raz, P. Ghisletta, K. M. Rodriguez, K. M. Kennedy, and U. Lindenberger, "Trajectories of brain aging in middle-aged and older adults: regional and individual differences," *Neuroimage*, vol. 51, no. 2, pp. 501–511, 2010.

[54] S. G. Popescu, B. Glocker, D. J. Sharp, and J. H. Cole, "Local brain-age: a u-net model," *Frontiers in Aging Neuroscience*, vol. 13, p. 761954, 2021.

[55] N. Gianchandani, M. Dibaji, J. Ospel, F. Vega, M. Bento, M. E. MacDonald, and R. Souza, "A voxel-level approach to brain age prediction: A method to assess regional brain aging," *arXiv preprint arXiv:2310.11385*, 2023.

[56] A. Makropoulos, E. C. Robinson, A. Schuh, R. Wright, S. Fitzgibbon, J. Bozek, S. J. Counsell, J. Steinweg, K. Vecchiatto, J. Passerat-Palmbach *et al.*, "The developing human connectome project: A minimal processing pipeline for neonatal cortical surface reconstruction," *Neuroimage*, vol. 173, pp. 88–112, 2018.

[57] A. Makropoulos, I. S. Gousias, C. Ledig, P. Aljabar, A. Serag, J. V. Hajnal, A. D. Edwards, S. J. Counsell, and D. Rueckert, "Automatic whole brain mri segmentation of the developing neonatal brain," *IEEE transactions on medical imaging*, vol. 33, no. 9, pp. 1818–1831, 2014.

[58] A. Schuh, A. Makropoulos, R. Wright, E. C. Robinson, N. Tusor, J. Steinweg, E. Hughes, L. C. Grande, A. Price, J. Hutter *et al.*, "A deformable model for the reconstruction of the neonatal cortex," in *2017 IEEE 14th international symposium on biomedical imaging (ISBI 2017)*. IEEE, 2017, pp. 800–803.

[59] A. Kendall, Y. Gal, and R. Cipolla, "Multi-task learning using uncertainty to weigh losses for scene geometry and semantics," in *Proceedings of the IEEE conference on computer vision and pattern recognition*, 2018, pp. 7482–7491.

[60] W. Wang, E. Xie, X. Li, D.-P. Fan, K. Song, D. Liang, T. Lu, P. Luo, and L. Shao, "Pyramid vision transformer: A versatile backbone for

dense prediction without convolutions,” in *Proceedings of the IEEE/CVF international conference on computer vision*, 2021, pp. 568–578.

[61] ——, “Pvt v2: Improved baselines with pyramid vision transformer,” *Computational visual media*, vol. 8, no. 3, pp. 415–424, 2022.

[62] W. Yu, M. Luo, P. Zhou, C. Si, Y. Zhou, X. Wang, J. Feng, and S. Yan, “Metaformer is actually what you need for vision,” in *Proceedings of the IEEE/CVF conference on computer vision and pattern recognition*, 2022, pp. 10 819–10 829.

[63] N. Ottmakov, A. M. Shirke, and R. Malinow, “Measuring the impact of probabilistic transmission on neuronal output,” *Neuron*, vol. 10, no. 6, pp. 1101–1111, 1993.

[64] L. Aitchison and M. Lengyel, “The hamiltonian brain: Efficient probabilistic inference with excitatory-inhibitory neural circuit dynamics,” *PLoS computational biology*, vol. 12, no. 12, p. e1005186, 2016.

[65] C. E. Kelly, D. K. Thompson, C. L. Adamson, G. Ball, T. Dhollander, R. Beare, L. G. Matthews, B. Alexander, J. L. Cheong, L. W. Doyle *et al.*, “Cortical growth from infancy to adolescence in preterm and term-born children,” *Brain*, vol. 147, no. 4, pp. 1526–1538, 2024.

[66] M. Bouyssi-Kobar, J. Murnick, M. Brossard-Racine, T. Chang, E. Mahdi, M. Jacobs, and C. Limperopoulos, “Altered cerebral perfusion in infants born preterm compared with infants born full term,” *The Journal of Pediatrics*, vol. 193, pp. 54–61, 2018.

[67] G. Ball, L. Srinivasan, P. Aljabar, S. J. Counsell, G. Durighel, J. V. Hajnal, M. A. Rutherford, and A. D. Edwards, “Development of cortical microstructure in the preterm human brain,” *Proceedings of the National Academy of Sciences*, vol. 110, no. 23, pp. 9541–9546, 2013.

[68] W. Zheng, Z. Zhao, Z. Zhang, T. Liu, Y. Zhang, J. Fan, and D. Wu, “Developmental pattern of the cortical topology in high-functioning individuals with autism spectrum disorder,” *Human Brain Mapping*, vol. 42, no. 3, pp. 660–675, 2021.

[69] J. Seidlitz, F. Váša, M. Shinn, R. Romero-Garcia, K. J. Whitaker, P. E. Vértes, K. Wägstyl, P. K. Reardon, L. Clasen, S. Liu *et al.*, “Morphometric similarity networks detect microscale cortical organization and predict inter-individual cognitive variation,” *Neuron*, vol. 97, no. 1, pp. 231–247, 2018.

[70] T. Liu, F. Gao, W. Zheng, Y. You, Z. Zhao, Y. Lv, W. Chen, H. Zhang, C. Ji, and D. Wu, “Diffusion mri of the infant brain reveals unique asymmetry patterns during the first-half-year of development,” *NeuroImage*, vol. 242, p. 118465, 2021.

[71] V. Duboc, P. Dufourcq, P. Blader, and M. Roussigné, “Asymmetry of the brain: development and implications,” *Annual review of genetics*, vol. 49, no. 1, pp. 647–672, 2015.

[72] X.-Z. Kong, S. R. Mathias, T. Guadalupe, E. L. W. Group, D. C. Glahn, B. Franke, F. Crivello, N. Tzourio-Mazoyer, S. E. Fisher, P. M. Thompson *et al.*, “Mapping cortical brain asymmetry in 17,141 healthy individuals worldwide via the enigma consortium,” *Proceedings of the National Academy of Sciences*, vol. 115, no. 22, pp. E5154–E5163, 2018.

[73] K. W. Nam, N. Castellanos, A. Simmons, S. Froudast-Walsh, M. P. Allin, M. Walshe, R. M. Murray, A. Evans, J.-S. Muehlboeck, and C. Nosarti, “Alterations in cortical thickness development in preterm-born individuals: Implications for high-order cognitive functions,” *NeuroImage*, vol. 115, pp. 64–75, 2015.

[74] G. Mento, A. Suppiej, G. Altoè, and P. S. Bisiacchi, “Functional hemispheric asymmetries in humans: electrophysiological evidence from preterm infants,” *European Journal of Neuroscience*, vol. 31, no. 3, pp. 565–574, 2010.

[75] B. Schmitz-Koep, A. Menegaux, C. Gaser, E. Brandes, D. Schinz, M. Thalhammer, M. Daamen, H. Boecker, C. Zimmer, J. Priller *et al.*, “Altered gray matter cortical and subcortical t1-weighted/t2-weighted ratio in premature-born adults,” *Biological Psychiatry: Cognitive Neuroscience and Neuroimaging*, vol. 8, no. 5, pp. 495–504, 2023.

[76] Z. Zhang, C. Zhang, X. Zhang, Y. Xu, W. Dou, M. Li, W. Zheng, and B. Li, “Dynamic structure-function coupling in macroscale neonatal brain networks,” *Communications Biology*, 2025.

[77] R. Dimitrova, M. Pietsch, D. Christiaens, J. Ciarrusta, T. Wolfers, D. Batalle, E. Hughes, J. Hutter, L. Cordero-Grande, A. N. Price *et al.*, “Heterogeneity in brain microstructural development following preterm birth,” *Cerebral Cortex*, vol. 30, no. 9, pp. 4800–4810, 2020.

[78] S. Nivins, N. Padilla, H. Kvanta, and U. Ådén, “Gestational age and cognitive development in childhood,” *JAMA Network Open*, vol. 8, no. 4, pp. e254 580–e254 580, 2025.

[79] J. E. Kline, V. S. P. Illapani, L. He, M. Altaye, J. W. Logan, and N. A. Parikh, “Early cortical maturation predicts neurodevelopment in very preterm infants,” *Archives of Disease in Childhood-Fetal and Neonatal Edition*, vol. 105, no. 5, pp. 460–465, 2020.

[80] M. Hinojosa-Rodríguez, T. Harmony, C. Carrillo-Prado, J. D. Van Horn, A. Irimia, C. Torgerson, and Z. Jacokes, “Clinical neuroimaging in the preterm infant: diagnosis and prognosis,” *NeuroImage: Clinical*, vol. 16, pp. 355–368, 2017.